RSC Advances

PAPER

View Article Online
View Journal | View Issue

Check for updates

Cite this: *RSC Adv.*, 2025, **15**, 28145

Structure, magnetism and heating ability of pyrrole-functionalized magnetic biochar (PFMB) for magnetic hyperthermia

O. M. Lemine, *[a] M. Bououdina,[b] Turki Altoub,[a] M. Alshammari,[c] Kadi Y. Museery,[c] Ali Z. Alanzi[c] and Latifa Latrous[d]

This work reports the synthesis, characterization, and magnetic hyperthermia performance of pyrrole-functionalized magnetic biochar (PFMB) nanocomposites prepared *via* a hydrothermal method. The PFMB system comprises Fe_3O_4 nanoparticles embedded in a biochar matrix and coated with pyrrole to improve colloidal stability and heating efficiency. Structural and morphological analyses (XRD, FTIR, SEM/EDAX) confirmed the formation of a magnetite phase and successful surface functionalization. Magnetic measurements reveal a transition from ferrimagnetic behavior in bare MB to superparamagnetism in PFMB, with saturation magnetization reduced significantly from 58.8 to 20.8 emu g^{-1}. Magnetic hyperthermia experiments under alternating magnetic fields (AMF) manifest enhanced heating efficiency for PFMB, with sample absorption rate (SAR) values varying considerably from 24.27 to 53.77 W g^{-1}, compared to 12.34–31.80 W g^{-1} for MB. The results indicate that at higher frequencies (332 kHz and 469 kHz), both MNPs reach the therapeutic hyperthermia threshold of 42 °C in a relatively short time. The heating performance correlates well with both frequency and field amplitude. Intrinsic loss power (ILP) values for PFMB reach 0.70 nH m^2 kg^{-1}, aligning with the values reported for established polymer-coated MNPs. These results demonstrate the potential of PFMB nanocomposites as efficient and stable candidates for *in vitro* magnetic hyperthermia applications.

Received 11th June 2025
Accepted 30th July 2025

DOI: 10.1039/d5ra04120a

rsc.li/rsc-advances

Open Access Article. Published on 07 August 2025. Downloaded on 1/20/2026 9:40:54 AM.
This article is licensed under a Creative Commons Attribution-NonCommercial 3.0 Unported Licence.

1. Introduction

Pyrrole-functionalized magnetic biochar (PFMB) is a hybrid nanocomposite consisting of iron oxide magnetic nanoparticles (MNPs) embedded within a biochar matrix and subsequently coated with pyrrole. This configuration has attracted growing interest for biomedical applications, particularly in magnetic hyperthermia (MH) therapy for cancer, owing to its enhanced thermal efficiency and biocompatibility.[1,2] Under an AMF, the magnetic core acts as a nano-heater, converting electromagnetic energy into heat *via* magnetic relaxation processes.

Pyrrole coating plays a pivotal role in maintaining colloidal stability by mitigating MNP agglomeration, which is a requirement for enhanced heating efficiency of MNPs and for an efficient MH.[3] Furthermore, the functionalization of magnetic biochar (MB) with naturally derived caffeic acid introduces surface hydroxyl and carboxyl groups, thus enhancing aqueous dispersibility and biocompatibility while offering potential sites for drug loading or molecular targeting.[4,5]

The heat generation capability of MNPs under AMF is governed primarily by two relaxation mechanisms: Néel relaxation, involving the reorientation of magnetic moments within the crystal lattice, and Brownian relaxation, in which the entire particle rotates in suspension to follow the magnetic field.[6] The efficiency of each mechanism depends on several factors such as particle size, magnetic anisotropy, and matrix confinement. In the PFMB system, both the pyrrole shell and biochar scaffold influence these mechanisms by controlling particle mobility and interparticle interactions. Notably, the pyrrole coating prevents aggregation and maintains interparticle separation, which is crucial to sustaining efficient magnetic relaxation.[7] Numerous studies have highlighted the multifunctional advantages of pyrrole-coated MNPs, including improved heating efficiency, enhanced dispersion in aqueous media, and increased thermal stability.[2,8,9] For instance, Mol *et al.*[2] demonstrated that Fe_3O_4 MNPs coated with pyrrole exhibit enhanced biocompatibility and tunable heating capacity. Bao *et al.*[8] reported SAR of 1648 W g^{-1} for pyrrole-coated magnetite nanorings subjected to simultaneous AMF and near-infrared (NIR) irradiation, along with negligible cytotoxicity. Similarly, Sethulakshimi *et al.*[9] found that plasma polymerization of

[a]*Department of Physics, College of Sciences, Imam Mohammad Ibn Saud Islamic University (IMISU), Riyadh 11623, Saudi Arabia. E-mail: mamamin@imamu.edu.sa*
[b]*Department of Mathematics and Sciences, College of Humanities and Sciences, Prince Sultan University, 11586 Riyadh, Saudi Arabia*
[c]*Microelectronics and Semiconductors Institute, King Abdulaziz City for Science and Technology (KACST), Riyadh, Saudi Arabia*
[d]*Laboratoire de Chimie Minérale Appliquée (LR19ES02), Faculté Des Sciences de Tunis, Université de Tunis El Manar, Campus Universitaire El Manar I, 2092 Tunis, Tunisie*

© 2025 The Author(s). Published by the Royal Society of Chemistry

Open Access Article. Published on 07 August 2025. Downloaded on 1/20/2026 9:40:54 AM.
This article is licensed under a Creative Commons Attribution-NonCommercial 3.0 Unported Licence.

polyaniline on iron oxide nanoparticles led to increased saturation magnetization and improved biocompatibility.

While substantial advances have been achieved in the development of polymer-coated magnetic nanoparticles (MNPs) for magnetic hyperthermia—particularly with coatings such as poly(acrylic acid) (PAA), polyethylene glycol (PEG), dextran, hyaluronic acid, chitosan, and polyvinylpyrrolidone (PVP)[10–13]—there remains a notable gap in systematic investigations focused on the magnetothermal performance of pyrrole-coated MNPs. Despite the promising conductive and stabilizing properties of pyrrole, its potential as a surface functionalization agent for enhancing heat dissipation efficiency in magnetic hyperthermia is still underexplored.

Motivated by recent work in which MB and PFMB MNPs were successfully synthesized *via* a hydrothermal approach for sensing applications,[14] we extended our investigation to evaluate their magnetothermal properties. In this study, MB and PFMB were fully characterized by X-ray diffraction (XRD), Fourier-transform infrared spectroscopy (FTIR), scanning electron microscopy with energy-dispersive X-ray analysis (SEM/EDAX), and superconducting quantum interference device (SQUID) magnetometry.

To assess their performance in magnetic hyperthermia, the specific absorption rate (SAR) was measured under varying alternating magnetic field (AMF) frequencies and field strengths. This study provides new insights into the role of pyrrole surface modification in optimizing the heating efficiency of MNPs for theranostic applications.

2. Experimental

2.1. Synthesis of PFMB nanocomposite

The synthesis procedure of the nanocomposite has been previously detailed in previous work, as illustrated in Fig. 1.[14] Briefly, the shells were cut into small fragments and thoroughly washed with distilled water to remove impurities and residual contaminants. After cleansing, the biomass was dehydrated in a hot-air oven at 80 °C for 24 h. The dried material was then finely ground using an electric grinder to yield a homogeneous powder.

To synthesize PFMB, the carbon precursor was mixed with iron(III) chloride hexahydrate ($FeCl_3 \cdot 6H_2O$), polyethylene glycol (PEG), and pyrrole (Py). The mixture was subjected to ultrasonic dispersion for 1 h to ensure uniform mixing with a Py/Fe molar ratio of 1.5. The resulting suspension was transferred into a 150 mL Teflon-lined autoclave and subjected to hydrothermal treatment at 180 °C for 17 h in a hot-air oven. The final product was collected as a dry powder.

2.2. Characterization

X-ray diffraction (XRD) patterns were recorded on a PROTO Benchtop powder diffraction system equipped with Cu Kα radiation source ($\lambda = 1.5418$ Å) and under the operating conditions: voltage of 30 V, current of 20 A, and power of 0.6 kW. The patterns were recorded in the 2θ range 20–80° using a scan rate of 0.015° and a counting time of 2 s. FTIR spectra were recorded using INFRALUM FT-08 ALUMEX in the wavenumber range 40–4000 cm^{-1}. Morphological observation and chemical

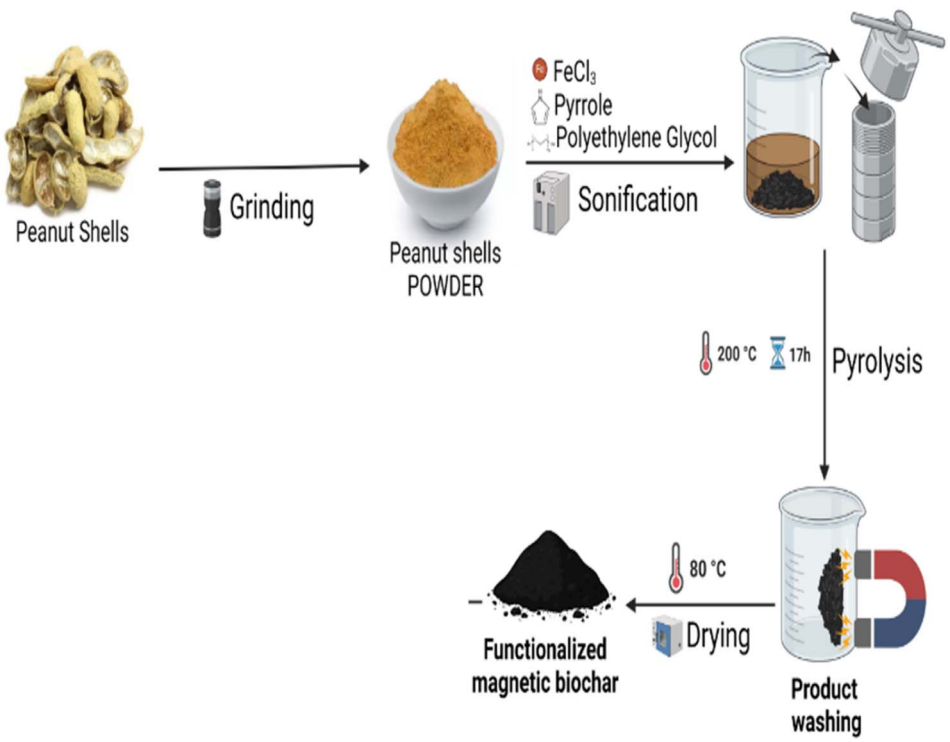

Fig. 1 Synthesis of Pyrrole Functionalized Magnetic Biochar (PFMB) nanocomposite (reproduced from our early work[14]).

© 2025 The Author(s). Published by the Royal Society of Chemistry

Open Access Article. Published on 07 August 2025. Downloaded on 1/20/2026 9:40:54 AM. This article is licensed under a Creative Commons Attribution-NonCommercial 3.0 Unported Licence.

composition were performed using SEM-SERON TECHNOLOGIES (Model, AIS 1800C). A Superconducting Quantum Interference Device (SQUID) magnetometer (San Diego, CA, USA) was used for the magnetic characterizations. A magnetic field of 100 Oe was applied to record zero-field-cooled and field-cooled (ZFC-FC) curves.

The heating efficiency of the samples was performed using a commercial system "Nanotherics Magnetherm". The SAR values are calculated by the following equation:

$$\mathrm{SAR} = \frac{\rho C_{\mathrm{w}}}{\mathrm{Mass}_{\mathrm{MNP}}}\left(\frac{\Delta T}{\Delta t}\right) \quad (1)$$

where C_{w} is the specific heat capacity of water (4.185 J g^{-1} K), ρ is the density of the colloid, $\mathrm{Mass}_{\mathrm{MNP}}$ is the concentration of the magnetic nanoparticles in the suspension and $\frac{\Delta T}{\Delta t}$ represents the heating rate. By performing a linear fit of temperature increase *versus* time at the initial time interval (1 to ~30 s), the slope $\Delta T/\Delta t$ is obtained.

3. Results and discussion

3.1. Structural, morphological and chemical composition characterizations

3.1.1. X-ray diffraction analysis. Fig. 2a depicts XRD patterns refined using the Rietveld method of magnetic biochar powders before and after pyrrole coating. It can be observed the presence of several broad peaks with a relatively low intensity, indicating the formation of nanocrystalline phase(s). These peaks are characteristic reflections (220), (311), (400), (422), (511), (440), and (533) of the magnetite phase Fe_3O_4 with an inverse spinel cubic structure (space group of $Fd\bar{3}m$, no. 225), in good agreement with JCPDS card no. 01-088-0315.

To further compute both structural and microstructural parameters, Rietveld refinements of the XRD patterns have been performed, see Fig. 2b and c. It is evident that the theoretical pattern based on the standard phase JCPDS card no. 01-088-0315 (blue curve) fits very well the experimental pattern (red curve), since the difference between the two curves (orange curve) gives almost a straight line. The goodness of fit parameter (S) is around 0.17. This indicates that the as prepared powdered samples are pure phases.

Table 1 summarizes the computed structural and microstructural parameters as obtained from the Rietveld refinements. It can be observed that the lattice parameter a is found to be 8.389 Å for magnetic biochar which decrease slight up to 8.379 Å for pyrrole coated magnetic biochar. This slight variation in the lattice parameter is usually associated with the local atomic arrangement (sites occupancy, vacancies), a typical behavior occurring within the inverse spinel cubic structure, where (Fe^{2+} with an ionic radius of 0.077 nm) occupies octahedral sites and (Fe^{3+} with an ionic radius of 0.063 nm) occupy tetrahedral sites. This effect has been widely reported in the literature and was found to have a direct effect on the magnetic properties,[16] since both ions have different magnetic moments, *i.e.* 4.89 μ_{B} for Fe^{2+} and 5.92 μ_{B} for Fe^{3+}.

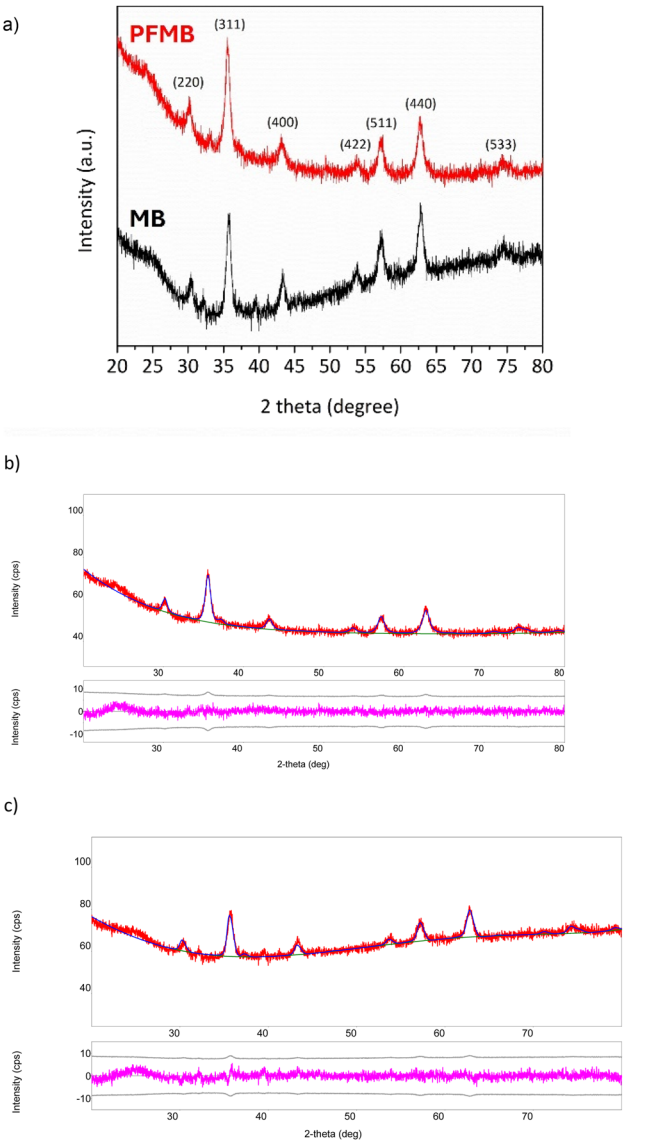

Fig. 2 (a) XRD diffraction of magnetic biochar powder before and after pyrrole coating, Rietveld refinements of (b) magnetic biochar and (c) biochar coated with pyrrole.

For microstructural parameters, it can be observed that the crystallite D size increases after coating, from 11.1 nm to 13.5 nm, due to the growth of a thin layer of pyrrole. Similarly, the microstrain ε increases significantly from 0.078% up to 0.711%. This is most probably originating from the coating of magnetic biochar with a polymeric layer of pyrrole compound.

3.1.2. FTIR analysis. The FTIR spectrum of Fe_3O_4/biochar exhibits a strong absorption band at approximately 587 cm^{-1} which correspond to the stretching vibrations of the Fe–O bond, confirming the presence of magnetite (Fig. 3). A broad absorption band centered around 3400 cm^{-1} is attributed to O–H stretching vibrations from hydroxyl groups and adsorbed water. The bands observed at 2920 and 2850 cm^{-1} could be assigned to C–H stretching vibrations of aliphatic groups. A band at 1630 cm^{-1} corresponds to the bending mode of adsorbed water molecules, while the peak at 1557 cm^{-1} is attributed to C=C

Open Access Article. Published on 07 August 2025. Downloaded on 1/20/2026 9:40:54 AM. This article is licensed under a Creative Commons Attribution-NonCommercial 3.0 Unported Licence.

Table 1 Structural and microstructural and fitting parameters computed from the Rietveld refinements of XRD patterns[a]

Sample	Phase composition (%)	Crystallite size D (nm)	Microstrain ε (%)	Lattice parameters (Å)	Fitting parameters
MB	Fe_3O_4 (magnetite)	11.1(1)	0.078(13)	$a = b = c = 8.389(1)$ $\alpha = \beta = \gamma = 90°$	$R_{wp} = 2.10\%$; $R_e = 12.37\%$; $R_p = 1.64\%$; $S = 0.1695$; $\chi^2 = 0.0287$
PFMB	Fe_3O_4 (magnetite)	13.5(1)	0.711(8)	$a = b = c = 8.379(2)$ $\alpha = \beta = \gamma = 90°$	$R_{wp} = 2.26\%$; $R_e = 14.17\%$; $R_p = 1.80\%$; $S = 0.1591$; $\chi^2 = 0.0253$

[a] R_{wp}: weighted profile R-factor; R_e: expected R-factor; R_p: profile R-factor; S: goodness of fit ($S = R_{wp}/R_e$); $\chi^2 = S^2$.

stretching, indicating the presence of aromatic structures in the biochar. The spectrum of the pyrrole-coated Fe_3O_4/biochar nanocomposite contains all characteristic peaks of Fe_3O_4 and biochar, along with additional bands attributed to the presence of polypyrrole. Notably, the Fe–O stretching vibration shifts slightly to 592 cm^{-1}, and an additional peak appears at ~628 cm^{-1}, suggesting modifications in the Fe_3O_4 environment due to coating. The band at 1542 cm^{-1}, associated with the C=C stretching in the pyrrole ring, shows increased intensity, indicating successful incorporation of polypyrrole. Additional pyrrole-specific vibrations include bands at 1458 cm^{-1} (symmetric stretching of the pyrrole ring and conjugated C–N bonds), 1376 and 1165 cm^{-1} (in-plane deformation and bending of C–H), and 1041 cm^{-1} (N–H in-plane deformation).

3.1.3. Morphological observations and chemical composition. The surface morphology and microstructure of the synthesized materials were examined *via* scanning electron microscopy (SEM), as shown in Fig. 4a–g. In Fig. 4a and 1b, bare Fe_3O_4 particles are observed with irregular, angular structures in the micron scale, indicating aggregated crystalline clusters. Upon compositing with biochar, the Fe_3O_4 particles appear to be embedded on the porous carbon matrix (Fig. 4c), suggesting improved dispersion and potential enhancement in surface area and stability. After coating with pyrrole, a substantial morphological transformation is observed (Fig. 4d and e), where Fe_3O_4 particles are uniformly encapsulated within a rough, interconnected polymeric network, forming spherical agglomerates with decreased particle definition. This indicates successful coating of Fe_3O_4 with pyrrole, which is further confirmed by higher magnification in (Fig. 4e). The particle size distribution histogram (Fig. 4f) derived from SEM analysis shows that the coated composite particles exhibit an average diameter of approximately 0.63 μm, indicating a relatively narrow and controlled size distribution. Furthermore, it is important to notice the values particle size estimated by SEM are different from the values of the crystallite size computed from the Rietveld analysis of XRD patterns. This indicates that each particle is in fact composed of several crystallites.

The high-magnification SEM image (Fig. 4g) further validates the coating of pyrrole on Fe_3O_4 within the pyrrole matrix, showing a core–shell-like structure with visible contrast differences. Adding this, the energy-dispersive X-ray spectroscopy (EDAX) elemental profile (Fig. 4h) confirms the presence of key elements including Fe, O, C thereby verifying the elemental composition of the composite. The strong Fe and O peaks indicate the magnetic core, while the presence of Cl and C supports pyrrole shell and possible doping elements. The detection of Na and minor atomic (At) peaks ascribed to residuals from the precursor or synthesis process. These morphological and compositional analyses collectively confirm the successful synthesis of a Fe_3O_4/biochar@pyrrole composite.

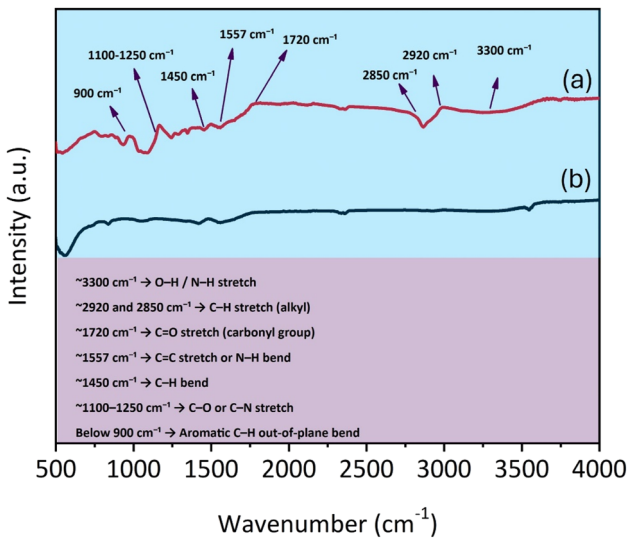

Fig. 3 FTIR spectra of (a) MB and (b) PFMB nanocomposites.

3.2. Magnetic properties

The magnetic behaviour of the MB and PFMB nanocomposites was comprehensively assessed through *M–H* hysteresis loops at 300 K and ZFC/FC magnetization measurements under a field of 100 Oe. As depicted in Fig. 4a, the MB sample exhibits a ferrimagnetic response, characterized by a noticeable coercivity and remanent magnetization, while the PFMB nanocomposite displays superparamagnetic behavior, evidenced by negligible coercivity and remanence (see inset of Fig. 5a). As shown in Fig. 5a, the MB MNPs do not reach magnetic saturation even at an applied field of 20 kOe. Therefore, the saturation magnetization (M_s) was estimated by applying the law of approach to saturation using the linear extrapolation of the *M versus* H^{-1} plot, resulting in an M_s of 58.8 emu g^{-1} (Fig. 5b). PFMB MNPs exhibit M_s of 20.8 emu g^{-1}, corresponding to a reduction of approximately 63% compared to the MB MNPs.

This significant decrease in M_s upon pyrrole coating is attributed to several factors, including.[12,13,15–17] (i) Interfacial

© 2025 The Author(s). Published by the Royal Society of Chemistry

Open Access Article. Published on 07 August 2025. Downloaded on 1/20/2026 9:40:54 AM.
This article is licensed under a Creative Commons Attribution-NonCommercial 3.0 Unported Licence.

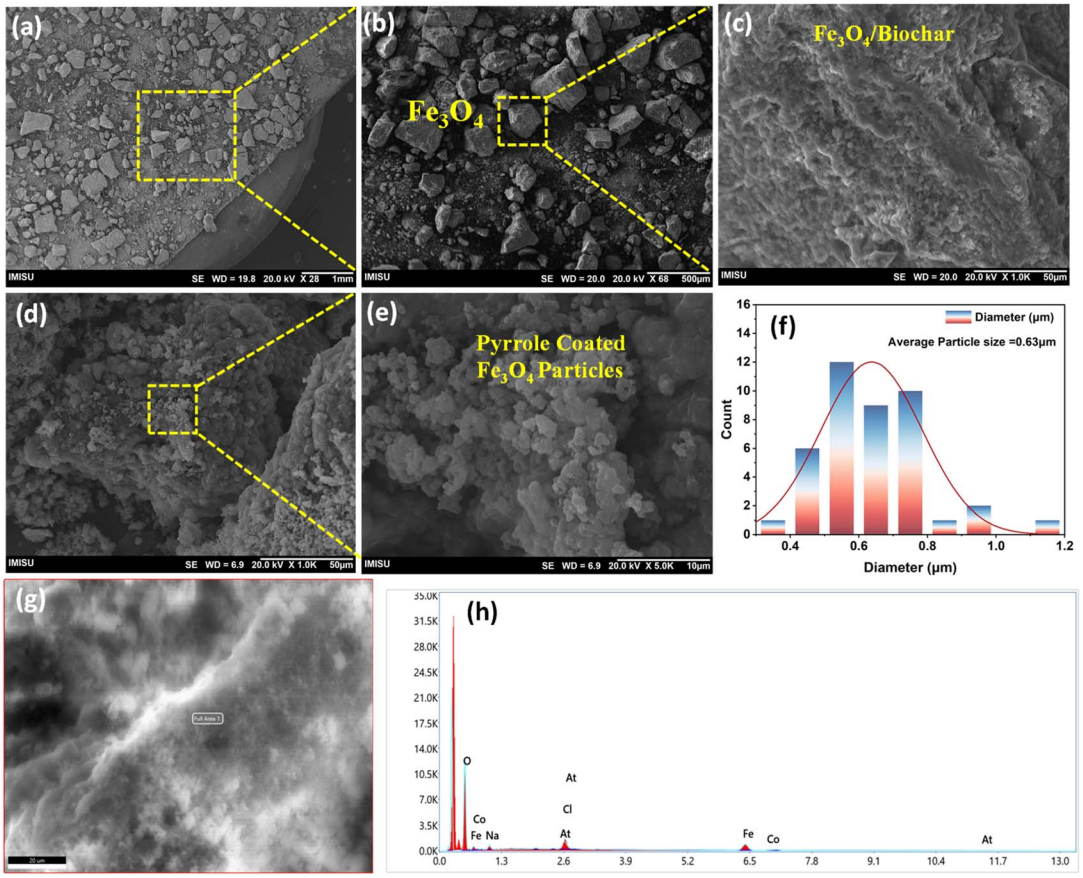

Fig. 4 SEM and compositional analysis of the synthesized composite materials: (a and b) low and higher magnification SEM images of pristine Fe_3O_4 particles showing angular and aggregated morphology. (c) Fe_3O_4 dispersed on biochar, indicating improved distribution. (d and e) pyrrole-coated Fe_3O_4 particles with spherical agglomerates and rough surface morphology. (f) Particle size distribution with an average diameter of ~0.63 μm. (g) SEM image showing core–shell structure of Fe_3O_4@PPy. (h) EDAX spectrum confirming the presence of Fe, Co, C, and Cl elements in the composite.

disruptions caused by the non-magnetic polymer shell, which weaken dipolar interactions and reduce the collective magnetic response; (ii) the coating process may also influence the cation distribution within the spinel lattice. The magnetic properties of spinel ferrites are strongly governed by the occupancy of Fe ions in tetrahedral and octahedral sites. Interaction of the

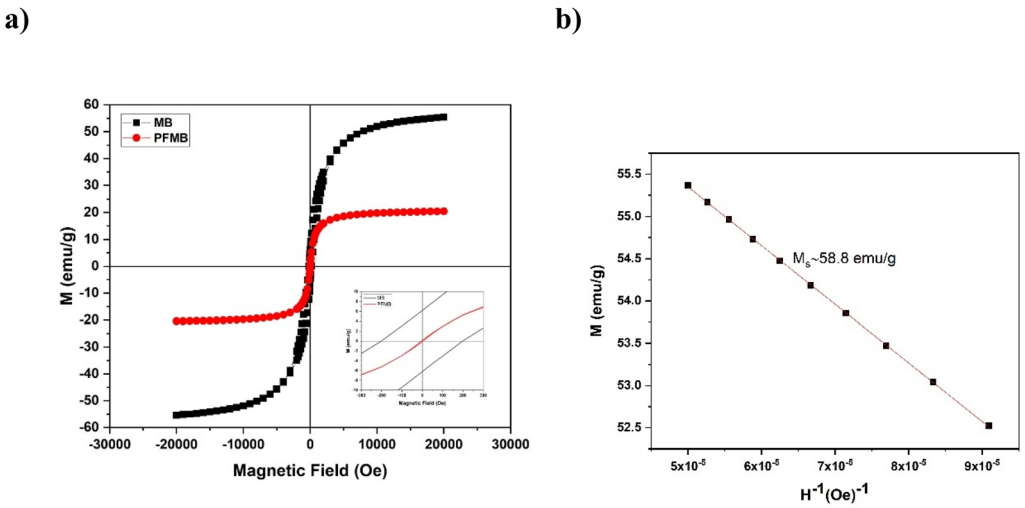

Fig. 5 (a) Room temperature *M*–*H* curves for the MB and PFMB MNPs. (bottom inset) Enlarged view of the *M*–*H* curves for the low field region and (b) extrapolated saturation magnetization for MB.

Open Access Article. Published on 07 August 2025. Downloaded on 1/20/2026 9:40:54 AM. This article is licensed under a Creative Commons Attribution-NonCommercial 3.0 Unported Licence.

polymer matrix with the particle surface during the coating procedure can induce local alterations in cation arrangement, affecting the superexchange interactions responsible for ferrimagnetic ordering. This interpretation is corroborated by XRD analysis, which confirmed an inverse spinel structure for the PFMB nanocomposite; and (iii) possible surface oxidation effects promoted by the functional groups of pyrrole, subtly impacting the Fe^{2+}/Fe^{3+} ratio and the overall magnetization.

These observations from *M–H* measurements are further supported by the ZFC/FC magnetization curves presented in Fig. 6a and b. The MB MNPs display a broad, gradual increase in the ZFC curve with no distinct blocking temperature (T_B), indicating a strong dipolar interaction, characteristic of clustered or multi-domain systems. In contrast, the PFMB exhibits a T_B around 290–300 K, reflecting a more uniform size distribution and effective magnetic decoupling provided by the pyrrole coating. This thermal behavior aligns well with the superparamagnetic nature of PFMB observed in the *M–H* curves at room temperature, confirming the stabilizing effect of the coating on the magnetic core and its role in reducing interparticle interactions.

To further verify the superparamagnetic behavior of the PFMB nanocomposite, the experimental $M(H)$ data were analyzed using the Langevin model of paramagnetism, described by the equation:

$$M = M_s\left(\coth\left(\frac{m_{np}H}{K_B T}\right) - \frac{K_B T}{m_{np}H}\right) \quad (2)$$

where M_s stands for saturation magnetization, m_{np} for magnetic moment, μ_0 for free-space permeability, K_B for the Boltzmann constant, T for temperature, and H for the applied magnetic field.

The experimental data showed an excellent agreement with the Langevin model, as evidenced by a coefficient of determination $R^2 = 0.998$, as illustrated in Fig. 7. This high correlation further confirms that the PFMB nanocomposite exhibits a superparamagnetic response at room temperature, dominated by the thermal fluctuation of non-interacting magnetic moments, and consistent with *M–H* loop characteristics.

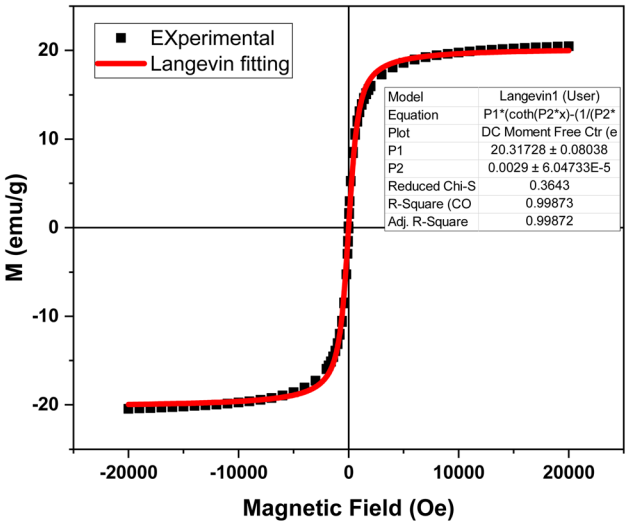

Fig. 7 Langevin fitting of magnetization of PFMB at 300 K

It can be concluded from the detailed magnetic study that while the pyrrole coating substantially reduces the saturation magnetization, it effectively enhances the superparamagnetic response and thermal stability of the nanocomposite, properties that are crucial for magnetic hyperthermia application.

3.3. Magnetic hyperthermia study

Fig. 8a–c depicts the temperature rise of aqueous dispersions of MB and PFMB with a fixed alternating magnetic field (AMF) amplitude of 170 Oe under different frequencies. The dispersions, with the concentration of 10 mg mL^{-1}, exhibit a significant temperature rise, achieving the therapeutic hyperthermia threshold of 42 °C at higher frequencies of 332 kHz and 469 kHz for both MNPs, which is essential for effective cancer treatment.

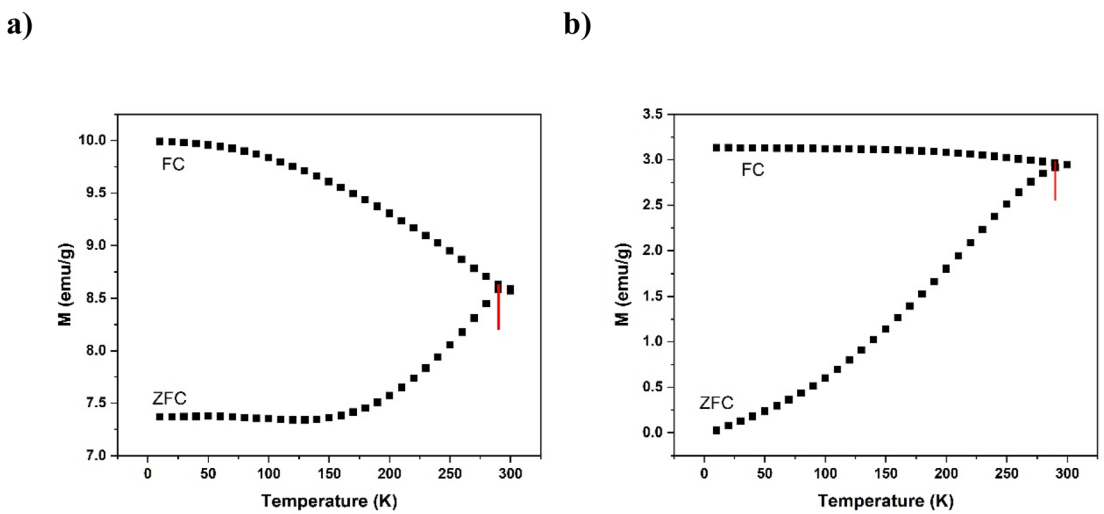

Fig. 6 The ZFC-FC magnetization measured under the field of 100 Oe for (a) MB and (b) PFMB MNPs.

© 2025 The Author(s). Published by the Royal Society of Chemistry

Open Access Article. Published on 07 August 2025. Downloaded on 1/20/2026 9:40:54 AM.
This article is licensed under a Creative Commons Attribution-NonCommercial 3.0 Unported Licence.

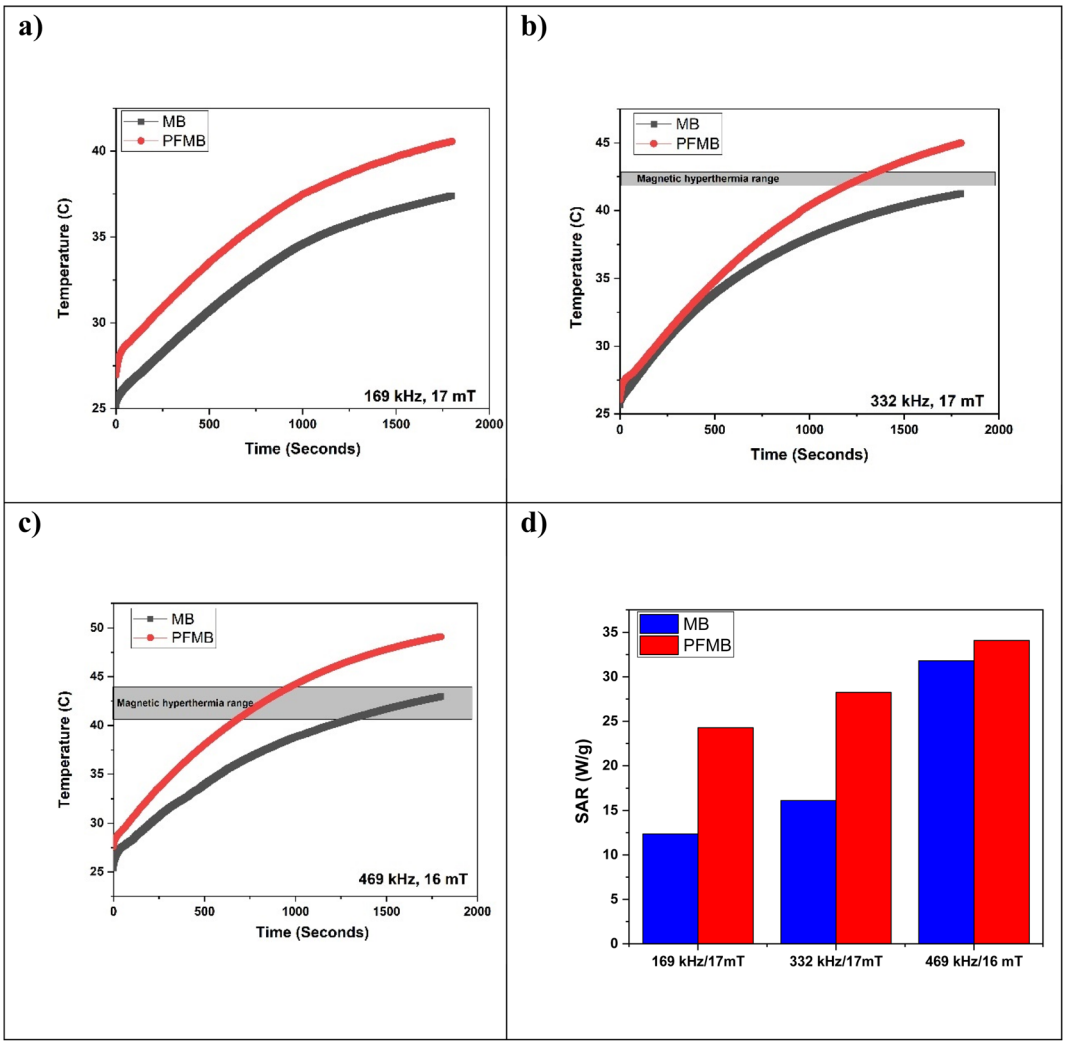

Fig. 8 (a–c) Temperature rise at different frequency for MB and PFMB and (d) corresponding SARs values for both MNPs.

In contrast, at lower frequencies (113 kHz and 170 kHz), neither MNPs system attains the hyperthermia threshold within the experimental timeframe, indicating their limited heating efficiency under such conditions. Quantitative analysis of the heating performance through specific absorption rate (SAR) (Table 2) revealed a clear enhancement following surface functionalization.

For MB MNPs, SAR values ranged from 12.34 W g^{-1} to 31.80 W g^{-1}, while the PFMB exhibited notably higher SAR values, in the range 24.27 W g^{-1} to 53.77 W g^{-1} across the studied frequencies. The enhanced SAR values observed for PFMB can be attributed to several factors. (i) The pyrrole surface functionalization likely improves colloidal stability by mitigating agglomeration, thereby facilitating more efficient heat dissipation. Furthermore, the superparamagnetic behavior of PFMB, as confirmed by magnetic characterization, reduces interparticle magnetic interactions that typically hinder heating performance. It is well known that heat dissipation under an AMF for superparamagnetic MNPs arises from Néel and Brownian relaxations. (ii) The presence of pyrrole reduces magnetic interactions between nanoparticles, which in turn affects the Néel relaxation time—potentially enhancing the heating efficiency. Brownian relaxation may also become faster due to improved dispersion and reduced aggregation. While these factors contribute positively to the heating performance, it is important to note that the overall magnetization tends to decrease due to the pyrrole coating, which can partially offset the heat generation. (iii) The mesoporous and carbonaceous framework of biochar improve heat dissipation by providing a thermally conductive scaffold that improves the overall magnetothermal conversion efficiency. This conductive network

Table 2 SAR and ILP for MB and PFMB MNPs

Samples	Frequency (kHz)	Field (mT)	SAR (W g^{-1})	ILP (nH m^2 kg^{-1})
MB	169	17	12.34	0.39
	332	17	16.11	0.26
	469	16	31.8	0.41
PFMB	169	17	24.27	0.78
	332	17	28.24	0.46
	469	16	53.77	0.70

Open Access Article. Published on 07 August 2025. Downloaded on 1/20/2026 9:40:54 AM.
This article is licensed under a Creative Commons Attribution-NonCommercial 3.0 Unported Licence.

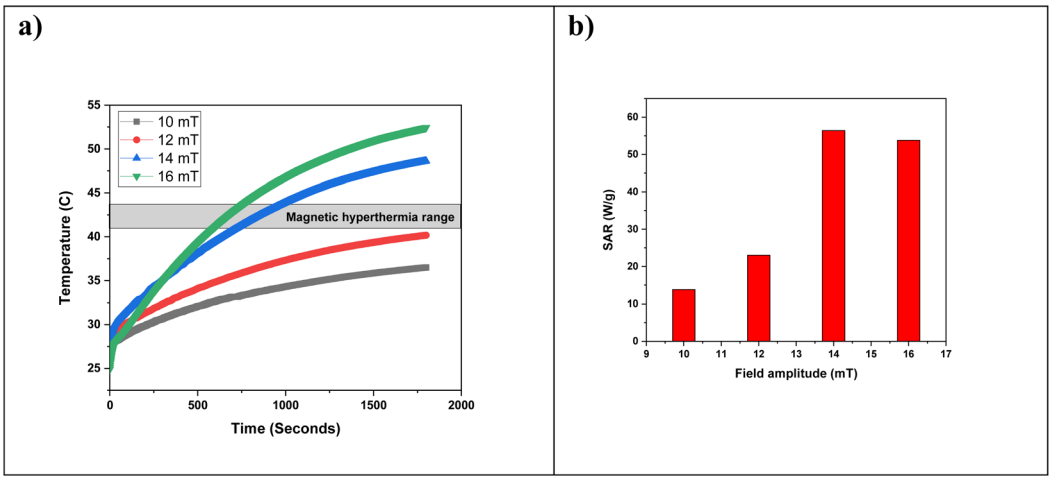

Fig. 9 (a)Temperature rise at different field amplitude and frequency of 469 kHz for PFMB and (b) SAR values.

also helps dissipate localized heat from individual nanoparticles across a broader volume, minimizing thermal hotspots and supporting a more homogeneous temperature rise during hyperthermia treatment. These effects synergistically contribute to the superior heating capability of PFMB compared to uncoated MB nanoparticles. Earlier studies have demonstrated that chitosan, dextran, PEG, PVP, and PAA coatings enhance heating properties of MNPs by improving dispersion and reducing interparticle magnetic interactions.[19–23]

To assess the effect of magnetic field strength on the heating ability of PFMB MNPs, experiments were conducted at a fixed frequency of 469 kHz and concentration of 10 mg mL^{-1}, while varying the AMF amplitude (H = 10, 12, 14, and 16 mT). The corresponding temperature rises are illustrated in Fig. 9a. The results clearly demonstrate that the temperature rise is highly dependent on the field amplitude. At lower field strengths (10 mT and 12 mT), the PFMB dispersions fail to reach the therapeutic hyperthermia threshold (42 °C) within the experimental duration, indicating insufficient heat generation under subthreshold field amplitudes. In contrast, at higher amplitudes (14 mT and 16 mT), the temperature surpasses 42 °C, confirming that high heating ability under these fields. This trend is further supported by the calculated SAR values (Fig. 9b), which exhibit a positive correlation with increasing field amplitude.

The maximum SAR observed for the PFMB nanocomposites in this study, 53.77 W g^{-1}, is within the upper range of SAR values reported for conventional polymer-coated iron oxide nanoparticles and is comparable to previously published values for similarly synthesized MNP systems (see Table 3). However, this value remains substantially lower than the exceptionally high SAR of 1648 W g^{-1} reported for pyrrole-coated magnetite nanorings subjected to simultaneous AMF and near-infrared (NIR) irradiation, a dual-stimulus strategy known to enhance hyperthermic performance through combined magnetothermal and photothermal effects.[8]

It is essential to emphasize that direct comparisons of SAR values across different studies must be approached with caution, as SAR is not an intrinsic material property but rather a function of numerous experimental and physical variables. Critical parameters influencing SAR include nanoparticle size and morphology, coating nature, magnetic anisotropy, and saturation magnetization, as well as external field parameters such as field amplitude (H), frequency (f). Additionally, calorimetric methods, sample holders, and data processing protocols vary across laboratories, contributing to systematic discrepancies in reported values.

For a more reliable comparison of heating efficiencies reported across different magnetic hyperthermia studies, the concept of Intrinsic Loss Power (ILP) has been introduced. Unlike the specific absorption rate (SAR), which is strongly influenced by experimental parameters such as field amplitude and frequency, ILP offers a normalized metric that facilitates

Table 3 Comparison of SAR values for different polymeric MNPs

Synthesis method	Composition	Field (kA m^{-1})	Frequency (kHz)	SAR (W g^{-1})	ILP (nH m^2 kg^{-1})	Reference
Hydrothermal	Pyrole-Fe_3O_4	17	469	53.77	0.46	This work
Hydrothermal	Fe_3O_4-PVP	17	332	160	0.6	19
Co-precipitation	Fe_3O_4-NH_4HCO_3	17.1	386.5	69.6	0.613	20
Emulsion polymerization	Fe_3O_4-PDMAEMA	20.25	260	~25	~0.4	21
Co-precipitation	Fe_3O_4-Chitosan	10–20	100	~20	~0.3	22
Hydrothermal	Fe_3O_4-PAA	17	332	36	0.59	23
Hydrothermal	Fe_3O_4-PEG	332	17	70	~0.55	19

© 2025 The Author(s). Published by the Royal Society of Chemistry

Open Access Article. Published on 07 August 2025. Downloaded on 1/20/2026 9:40:54 AM. This article is licensed under a Creative Commons Attribution-NonCommercial 3.0 Unported Licence.

objective evaluation of the intrinsic heating efficiency of magnetic nanoparticles.

It can be determined using the following expression:

$$\mathrm{ILP} = \mathrm{SAR}/fH^2 \quad (3)$$

where SAR is the specific absorption rate (W g^{-1}), H represents the applied field amplitude (A m^{-1}), and f denotes the applied frequency (Hz).

The resulting ILP is expressed in nH m^2 kg^{-1} and reflects the intrinsic ability of MNPs to convert electromagnetic energy into heat, independent of the applied field conditions.

As shown in Table 3, the ILP values obtained for PFMB MNPs fall within the range reported for similar polymer-coated MNP systems[21–25] and are comparable to those of commercial ferrofluids, which typically exhibit ILP values between 0.2 and 3.1 nH m^2 kg^{-1}.[26] These values reflect the relatively high intrinsic heating efficiency of PFMB under alternating magnetic field conditions, supporting their promising potential for *in vitro* magnetic hyperthermia applications.[18]

4. Conclusion

In this study, PFMB nanocomposites were successfully synthesized and characterized using a hydrothermal approach. The incorporation of Fe_3O_4 nanoparticles into a biochar matrix, followed by pyrrole surface coating, yielded a hybrid system with enhanced stability and less agglomeration. Comprehensive characterization confirmed the formation of an inverse spinel magnetite phase and effective polymer encapsulation. Magnetic measurements at room temperature demonstrated a transition from ferrimagnetism in bare MB to superparamagnetic behavior in PFMB, accompanied by a notable reduction in saturation magnetization due to the surface coating. Magnetic hyperthermia experiments revealed substantially improved heating performance in PFMB, with SAR values reaching up to 53.77 W g^{-1}, significantly exceeding those of uncoated MB. Both MNNPs reached the therapeutic hyperthermia threshold of 42 °C at higher AMF frequencies (332 kHz and 469 kHz). Furthermore, the calculated intrinsic loss power (ILP) values, as high as 0.70 nH m^2 kg^{-1}, fall within the performance range of polymer-coated iron oxide nanoparticles reported in the literature. These results highlight the critical role of pyrrole functionalization in enhancing magnetothermal efficiency by improving dispersion and reducing magnetic interaction. The PFMB nanocomposite emerges as a promising candidate for *in vitro* magnetic hyperthermia, with potential further development in theranostic applications.

Conflicts of interest

There are no conflicts to declare.

Data availability

All authors declare that all data of the paper are available on request.

Acknowledgements

This work was supported and funded by the Deanship of Scientific Research at Imam Mohammad Ibn Saud Islamic University (IMSIU) (grant number IMSIU-DDRSP2501).

References

1 Q. Zhuo, *et al.*, Applications of biochar in medical and related environmental fields: current status and future perspectives, *Carbon Res.*, 2023, **2**, 32.
2 B. Mol, *et al.*, Radio frequency plasma assisted surface modification of Fe_3O_4 nanoparticles using polyaniline/polypyrrole for bioimaging and magnetic hyperthermia applications, *J. Mater. Sci.:Mater. Med.*, 2021, **32**(9), 108.
3 P. Sun, *et al.*, Efficient removal of crystal violet using Fe_3O_4-coated biochar: the role of the Fe_3O_4 nanoparticles and modeling study their adsorption behavior, *Sci. Rep.*, 2015, **5**, 12638.
4 J. Lee, *et al.*, Caffeic acid-coated multifunctional magnetic nanoparticles for the treatment and bimodal imaging of tumours, *J. Photochem. Photobiol., B*, 2016, **160**, 210–216.
5 C. Magnani, *et al.*, Caffeic acid: a review of its potential use in medications and cosmetics, *Anal. Methods*, 2014, **6**(10), 3203–3210.
6 O. Lemine, *et al.*, Effect of Magnesium Ion Substitution on Physical Properties and Magnetic Induction Heating of Maghemite (γ-Fe2O3) Nanoparticles, *J. Supercond. Novel Magn.*, 2023, **36**(6), 1583–1593.
7 O. M. Lemine, *et al.*, Enhanced in vitro magnetic hyperthermia performance of chitosan-coated $CoFe_2O_4$ nanoparticles, *Mater. Today Commun.*, 2025, **46**, 112852.
8 J. Bao, *et al.*, Polypyrrole-Coated Magnetite Vortex Nanoring for Hyperthermia-Boosted Photothermal/Magnetothermal Tumor Ablation Under Photoacoustic/Magnetic Resonance Guidance, *Front. Bioeng. Biotechnol.*, 2021, **9**, 721617.
9 N. Sethulakshimi, *et al.*, Contact potential induced enhancement of magne tization in polyaniline coated nanomagnetic iron oxides by plasma polymerization, *Appl. Phys. Lett.*, 2013, **103**, 162414.
10 K. El-Boubbou, *et al*, Evaluating magnetic and thermal effects of various polymerylated magnetic iron oxide nanoparticles for combined chemo-hyperthermia, *New J. Chem.*, 2022, **46**, 5489–5504.
11 N. D. Thorat, *et al.*, Superparamagnetic iron oxide nanocargoes for combined cancer thermotherapy and MRI applications, *Phys. Chem. Chem. Phys.*, 2016, **18**(31), 21331–21339.
12 I. Anila, *et al.*, Synthesis and magneto-structural properties of chitosan coated ultrafine cobalt ferrite nanoparticles for magnetic fluid hyperthermia in viscous medium, *Ceram. Int.*, 2022, **48**(16), 22767–22781.
13 K. El-Boubbou, *et al.*, Preparation and characterization of various PVPylated divalent metal-doped ferrite nanoparticles for magnetic hyperthermia, *RSC Adv.*, 2024, **14**, 15664–15679.

Open Access Article. Published on 07 August 2025. Downloaded on 1/20/2026 9:40:54 AM.
This article is licensed under a Creative Commons Attribution-NonCommercial 3.0 Unported Licence.

14 I. Abidli, *et al.*, Electrochemical sensing of caffeic acid on natural biomass-pyrrole-functionalized magnetic biochar (PFMB) as promising SPE material, *Microchim. Acta*, 2025, **192**, 239.
15 K. El-Boubbou, *et al.*, Preparation and characterization of various PVPylated divalent metal-doped ferrite nanoparticles for magnetic hyperthermia, *RSC Adv.*, 2024, **14**, 15664–15679.
16 T. Wu, *et al.*, Preparation and characterization of magnetic ferrite-chitosan nanoparticles delivery for DOX, *Inorg. Chim. Acta*, 2024, **559**, 121791.
17 S. Shokri, *et al.*, Synthesis and characterization of a novel magnetic chitosan–nickel ferrite nanocomposite for antibacterial and antioxidant properties, *Sci. Rep.*, 2023, **13**(1), 15777.
18 B. Aslibeiki, *et al.*, Solvothermal synthesis of $MnFe_2O_4$ nanoparticles: the role of polymer coating on morphology and magnetic properties, *J. Magn. Magn. Mater.*, 2016, **399**, 236–244.
19 K. El-Boubbou, *et al.*, Evaluating magnetic and thermal effects of various Polymerylated magnetic iron oxide nanoparticles for combined chemo-hyperthermia, *New J. Chem.*, 2022, **46**, 5489–5504.
20 A. Radoń, *et al.*, Influence of the modifiers in polyol method on magnetically induced hyperthermia and biocompatibility of ultrafine magnetite nanoparticles, *Sci. Rep.*, 2023, **13**, 7860.
21 F. Reyes-Ortega, *et al.*, Magnetic Nanoparticles Coated with a Thermosensitive Polymer with Hyperthermia Properties, *Polymers*, 2018, **10**(1), 10.
22 E. Catalano and A. Di Benedetto, IOP Conf. Series, *J. Phys.:Conf. Ser.*, 2017, **841**, 012010.
23 S. Algessair, *et al.*, Tuning the heat dissipated by polyacrylic acid (PAA)-coated magnetite nanoparticles under alternating magnetic field for hyperthermia applications, *Appl. Phys. A*, 2023, **129**, 814.
24 P. De la Presa, *et al.*, Study of heating efficiency as a function of concentration, size, and applied field in γ-Fe_2O_3 nanoparticles, *J. Phys. Chem. C*, 2012, **116**(48), 25602–25610.
25 S. Matsuda, *et al.*, Synthesis of cobalt ferrite nanoparticles using spermine and their effect on death in human breast cancer cells under an alternating magnetic field, *Electrochim. Acta*, 2015, **183**, 153–159.
26 M. Kallumadil, *et al.*, Suitability of commercial colloids for magnetic hyperthermia, *J. Magn. Magn. Mater.*, 2009, **321**(10), 1509–1513.

© 2025 The Author(s). Published by the Royal Society of Chemistry